Petroleum Science and Engineering
2025, Vol. 9, No. 1, pp. 22-37
https://doi.org/10.11648/j.pse.20250901.13

Case Report

Calibrated 3D Geomechanical Model for Forecasting Gas Storage Seismicity

Cas Berentsen*, Hans De Pater

Fenix Consulting Delft BV, Delft, The Netherlands

Abstract

The Bergermeer reservoir is one of the largest gas storages in Western-Europe, with excellent reservoir properties. However, during original depletion seismicity was observed with magnitude up to 3.5 at a pressure below 58 bar. Therefore, it was deemed prudent to monitor the gas storage reservoir with a permanent, downhole micro-seismic array. The monitoring is embedded in a so-called Traffic Light System for managing seismic activity. The array observed 400 micro-seismic events with a magnitude below 0.9 during refill of the reservoir. Most activity was induced by the Midfield fault that also induced depletion seismicity. This activity is far below the threshold for felt or damaging earthquakes. A calibrated geomechanical model was developed that matches the micro-seismicity observed during refill and storage cycles. The geometry was obtained from the seismic interpretations using an efficient method to convert the faults and horizons to parametric surfaces that can be used in a Finite Element Method (FEM) model. The model was populated with Leak-off Test (LOT), minifrac, core and log data. The model was calibrated on observed depletion and refill seismicity, stress measurements and the observed surface displacement from geodetic and GPS surveys. The continuous records of surface displacements showed a much stiffer reservoir during refill, compared with depletion. Also, the response was delayed by 0.25 year with respect to pressure, indicating time dependence in the rock deformation. Fault slip during depletion and stress hysteresis explains the refill micro-seismicity, since the peak shear stress is redistributed during slippage, giving higher shear stress at the edges of the slip area. The model predicts higher seismic activity for higher injection rate, but the maximum magnitude is limited in the worst case to 2.2, which is expected to cause no damage.

Keywords

Gas Storage, Seismicity, Calibrated Geomechanical Model, Passive Seismic Monitoring, Subsidence Monitoring

1. Introduction

Concern about seismic risk in Bergermeer arose since the reservoir induced significant earthquakes of magnitude up to 3.5, causing some minor damage to houses. These earthquakes occurred during the depletion phase that lasted till 2007 when the gas field had been depleted down to 20 bar. Figure 1 shows the pressure history and earthquakes. The earthquakes originated from the midfield fault that separates the two compartments [1].

When the reservoir was considered for gas storage, it was decided to first investigate the mechanism of seismicity and determine the seismic risk during refill of the gas reservoir and subsequent production-injection cycles.

*Corresponding author: hans.depater@fenixdelft.com (Cas Berentsen)

Received: 3 March 2025; **Accepted:** 14 March 2025; **Published:** 29 April 2025

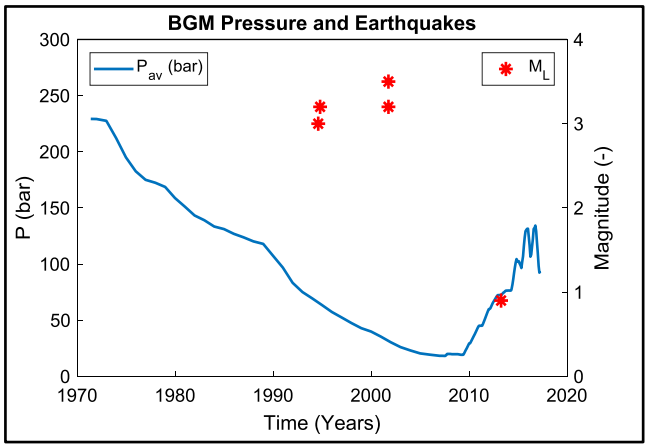

Figure 1. *Bergermeer pressure history and earthquakes. The strongest events occurred after depletion, but some four hundred micro-seismic events (below magnitude 0) were also observed during refill.*

Figure 2 shows micro-seismic activity vs. time and the average pressure and pressure difference between the east and west compartments (top graph). The cumulative seismic moment by fault system and injection and production rate are plotted in the lower graph. The plot of seismic moment (on a logarithmic scale) is useful since it will quickly level off with constant activity. If seismic activity becomes stronger such a plot will show a stair step pattern. Such a plot would flag a system that becomes gradually more critical.

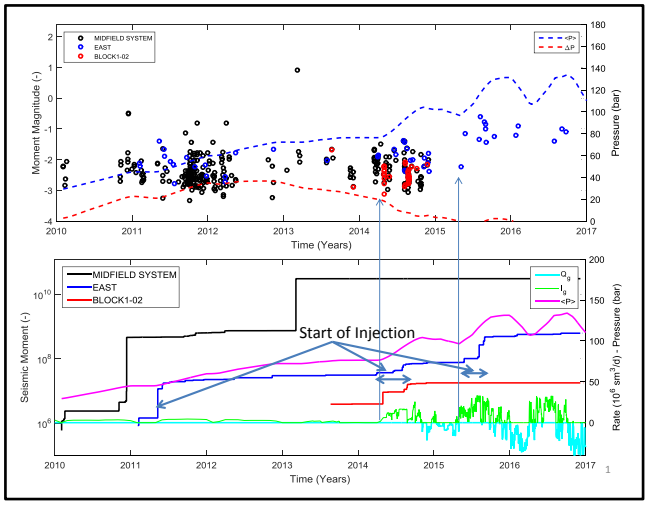

Figure 2. *Seismic activity in Bergermeer and pressure vs time (upper). Cumulative seismic moment and injection and production rate is plotted in the lower graph.*

Most events could be migrated to the main faults, shown in Figure 3, which is important for establishing the link between seismicity and geomechanical simulations, since the stress analysis in the geomechanical model is focused on the faults.

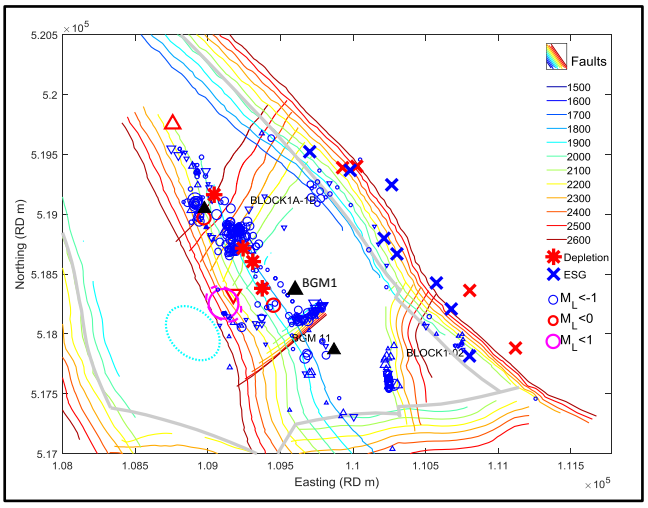

Figure 3. *Relocated events after migration to the faults. Mirror events that could not be resolved are indicated with up or down pointing triangles. Also, the assumed location of the depletion induced earthquakes is shown. The dashed magenta ellipse indicates the intersection of the uncertainty ellipsoid of the strongest event during cushion gas injection with a plane parallel to the fault plane through the original location.*

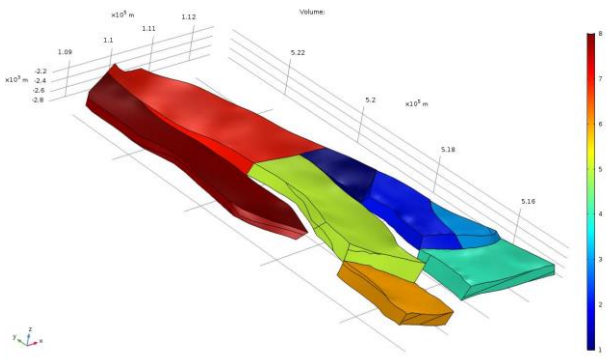

Figure 4. *Compartments of the Bergermeer reservoir; the cross section through the midfield fault is made at the point where the east and west compartments just separate.*

Since it is reasonable to consider the Midfield fault and BGM-11 and Block1A-1B faults in combination it does not matter very much for the analysis to which of these three faults the location was assigned. Moreover, from the micro-seismic analysis [2] it appears that events coming from these faults are strongly linked with one event triggering another on the crossing fault.

In Bergermeer a few relatively strong earthquakes happened during depletion and micro-seismic activity was observed during cushion gas injection, mainly on the Midfield fault. This continued with the first storage cycle but when average pressure reached around 100 bar, the activity on the Midfield fault system ceased and it has been quiet since.

Elastic models predict that the fault stress should immediately become stable when the pressure is increased during

cushion gas injection. However, a lot of micro-seismicity was observed, which agrees with laboratory testing on cores that shows not only micro-seismicity during loading, but also (declining) micro-seismic activity during unloading. Still, the strongest events up to magnitude 0.9 could be a warning of impending stronger seismicity, so the geomechanical model should explain the observed micro-seismicity.

The geomechanical reservoir model will be calibrated on the observed seismicity during depletion and refill, so that the model can be used to make a forecast of seismicity during future storage cycles.

In a 2D cross-section of the fault, we will show that the combination of rock stiffness and stress hysteresis and the stress re-distribution by slippage can explain the micro-seismicity during refill. In the 3D model the shear slippage has been modeled by adding the stress from the shear dislocation derived from the 2D model at the end of depletion. The model shows that at higher pressure the fault stabilizes so that any remaining seismicity will be weak during the storage cycles. The model will be used for the current maximum pressure of 133 bar, as well as a case with higher storage using maximum pressure of 150 bar.

2. Geomechanical Modelling

Previously, geomechanical models of Bergermeer were developed by [3, 4]. A new geomechanical model is constructed by creating fault blocks from the fault surfaces and intersecting those with horizons, based on a new seismic interpretation. The reservoir faults terminate at the Zechstein horizon and the underburden surface. Figure 5 shows the horizons used in the model in a cross-section through the scissor point of the Midfield fault; details of the modeling can be found in the full report [5].

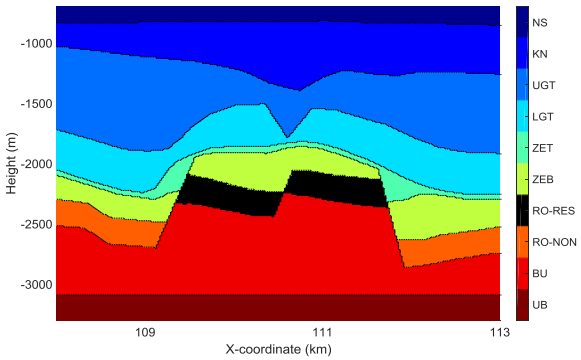

Figure 5. *Cross section perpendicular to the Midfield fault near the scissor point (i.e. the point south of which the eastern and western reservoir blocks are no longer juxtaposed), with indication of geological formations. North Sea (NS), top Vlieland Claystone (KN), top Upper Germanic Trias (UGT), top Lower Germanic Trias (LGT), top Zechstein Salt (ZET), Top Platten Dolomite and Anhydrite (ZEB), Top Rotliegend (RO), Top Carboniferous (BU) and the under burden (UB).*

The primary objective of the model is the computation of the fault stresses, which determines the extent of the horizons. The extent of the entire model is determined by the surface movement. This results in an inner domain that is roughly similar in size as the previous model [4].

2.1. Model Input Parameters

The geomechanical properties were based on input data from the previous models. The vertical stress is well constrained by density logs and reservoir pressure. The stress regime is normal with horizontal stresses less than vertical stress. Therefore, vertical and minimum horizontal stresses determine the shear stress and normal stress on the faults for potential fault slippage.

There are only two anchor points for the minimum horizontal stress: LOT's in the overburden and a minifrac in the reservoir in the depleted state. Figure 6 shows these measured data points together with the interpreted stress path. It is known from field cases with extensive stress measurements that reservoir stress is generally lower than shale stress, so the minimum stress is assumed lower than the LOT stress.

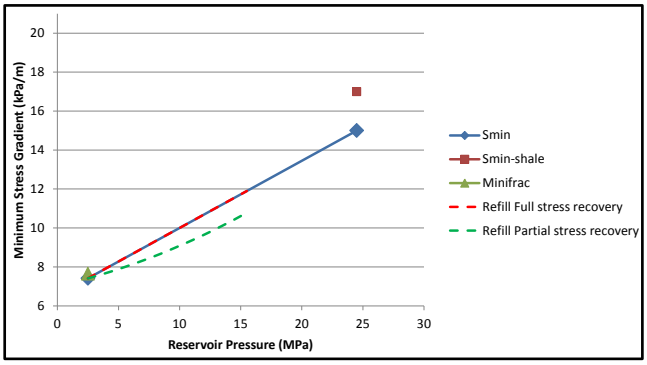

Figure 6. *Minimum stress gradient versus reservoir pressure inferred from LOT's and an injection test. Stress recovery is shown for two scenarios: linear stress path with full stress recovery (red dashed) and stress path with partial stress recover (green dashed).*

The stress recovery during refill and storage cycles is unknown and will be used as a free parameter that is calibrated against the observed micro-seismicity and surface displacement. Figure 6 gives an example for full and partial stress recovery. If partial stress recovery were to happen, the shear stress on the fault would become higher, giving more slip potential.

2.2. Eclipse Simulated Reservoir Pressure

The reservoir model was history matched until 2017. A reference forecast was made with a swing between 77 bar and 133 bar gas pressure. The Eclipse model output is used in the geomechanical simulation as input for the stress analysis. So, there is no flow simulation in the geomechanical model, but

the pressure distribution at selected time steps is applied as external stress on the reservoir domains.

3. Initialization, Calibration and Constitutive Model

The initial stresses are calibrated on the available data and the stress evolution is guided by theoretical relationships with 3 degrees of freedom that are strictly only valid for a 1D compaction model, i.e. a pancake reservoir that extends to infinity in the horizontal direction. The outcome of the stress is monitored so that the parameters could then be adjusted to achieve the required targets. The poro-elastic coefficient determines the stress change for given fluid pressure drop:

$$A_p = \alpha_B \frac{1-2\nu}{1-\nu} \tag{1}$$

The theoretical relationship for the Biot coefficient α_B reads

$$\alpha_B = \left(1 - c_g K\right) \tag{2}$$

Where C_g is the grain compressibility and k the bulk modulus.

The compaction coefficient C_m gives the vertical reservoir strain for given fluid pressure drop:

$$c_m = \frac{\alpha_B}{E} \frac{(1-2\nu)(1+\nu)}{1-\nu} = \frac{A_p}{2G} \tag{3}$$

Where G is the shear modulus.

Stresses are initialized in a three-step approach, with first determining vertical stress from density and then initializing horizontal stress from the horizontal stress ratio with subsequent equilibration. In this step, Maxwell visco-elasticity is applied to mimic salt creep so that shear stress concentrations are relieved. The step is repeated a few times to achieve the calibration targets for stresses that are:

1. Matching depletion stress path corresponding to the injection test performed in 2007
2. Isotropic stresses in the salt layer resulting from Salt creep over geological time.
3. Maximum horizontal over vertical stress ratio of 0.9 in all layers except for the salt, inferred from drilling experience in the area.

A minimum horizontal stress over vertical stress ratio between 0.68-0.69, except in the Anhydrite/Carbonate layer which has a stress ratio of 0.9. This higher value is required to accommodate for the stress concentrations resulting from the salt initialization.

The shear and normal stresses on the faults are mainly controlled by the minimum horizontal stress and vertical stress. The stress orientation coincides with the fault strike, which makes the model insensitive to the choice of the maximum horizontal stress. The minimum horizontal stress in the non-reservoir layers was calibrated on the critical fault behavior.

The measured subsidence shows a much stiffer response during refill and the storage cycles than during depletion. This is a commonly observed elastoplastic response with permanent deformation occurring during the first loading. The behavior could be modelled with an elastoplastic constitutive model, but this introduces unknowns that cannot be calibrated from independent data. To avoid this, the stiffer response was modelled with an inelastic response, using different elastic compaction moduli during refill compared with initial depletion. The different stages are combined using superposition of the increments. Such an approach violates energy conservation, because upon changing the modulus, the elastic deformation is not explicitly incorporated. However, it is a valid approach for the loading conditions of the reservoir since the average pressure after depletion is raised to a higher level. Compared with elastoplastic models this is equivalent to isotropic plasticity, which is the simplest approximation, using a constant stiffness below the maximum load level.

The time delay observed in the GPS measurements cannot be explained by the aquifer response present in the Eclipse model. This time delay indicates a viscoelastic response rather than an elastic response. The viscoelastic response is approximated with the Kelvin-Voigt (KV) model. The KV model describes a damper-spring system in parallel, where the response of the spring is delayed by a damper. Over time the influence of the damper diminishes and the response of the spring remains. The characteristic time scale for the damper is called the relaxation time. The relaxation time used will be a weighted averaged of the relaxation time observed in the 4 GPS stations. Because the characteristic time scale of the depletion phase is much longer than the delay time observed in the GPS measurement, the Kelvin-Voigt effect is not modelled during the depletion phase.

For the depletion phase the stress path is given by the stress measurements. For the refill and storage cycles the actual stress is unknown. However, it appears that the absence of large magnitude seismicity during refill and storage requires that the stress path in the middle of the reservoir fully recovers during the refill phase. The stress path is controlled by the poroelastic coefficient. Because the actual 3D response differs from the theoretical relationships, the poroelastic coefficient is used as a calibration parameter.

3.1. Parameter Calibration Matrix

Depletion and refill/storage were calibrated simultaneously; for both these phases three degrees of freedom control the Geomechanical response. In summary, for the depletion phase the compaction modulus follows from the subsidence (c_m=5 x 10^{-11} 1/Pa) and the poroelastic coefficient follows from the stress data in well BGM-8 (A_p=0.79). This leaves one degree

of freedom for the depletion phase for which the Poisson ratio is set. Because of the high poroelastic coefficient the choice for the Poisson ratio already is limited to the range [0, 0.175]. The choice will be further limited by the requirements for the refill and storage calibration. Once these parameters are set the Young's Modulus, Biot coefficient and grain compaction modulus follow from the theoretical relationships for the Biot coefficient, poroelastic coefficient and compaction modulus; Table 1 lists the calibration matrix.

Table 1. *Parameter calibration matrix. the grain compaction modulus c_g, the Poisson ratio v, the Young's modulus E, the Biot coefficient α_B, the Poroelastic coefficient A_p and the compaction modulus c_m, τ is the relaxation time for Kelvin-Voigt viscoelasticity.*

	A_p	c_m	v	c_g	E	α_B	τ
	(-)	**(1/Pa)**	**(-)**	**(1/Pa)**	**(GPa)**	**(-)**	**(days)**
Depletion 1971-2007	0.79	5×10^{-11}	Chosen	Follows	Follows	Follows	N/A
Refill + Storage 2007ff	Refill seismicity	2×10^{-11}	Follows	Same as for depletion	Follows	Follows	GPS data

For the refill and storage phase the stiffer compaction modulus follows from the Geodetic Survey and GPS measurements (c_m=2 x 10^{-11}1/Pa). The grain compaction modulus is expected to remain unaltered over the lifetime of the reservoir, which is determined by the depletion phase. The poroelastic coefficient during refill and storage is set such that stress fully recovers. It appears that this considerably narrows the range for the Poison ratio during depletion.

Finally the time delay observed in the surface movement by the GPS measurements is simulated with the viscoelastic Kelvin-Voigt model. The relaxation time in the model is matched to the observed GPS data.

3.2. Fault Stability Criterion: Predicting Seismicity

Since Dutch gas fields at virgin conditions have no critically stressed faults either at reservoir level or in the deep subsurface (as evidenced by absence of regular natural earthquakes), the most plausible mechanism for induced earthquakes is transfer of compaction strain to faults by differential compaction [6].

Since effective normal stress will increase due to depletion, the shear stress caused by differential compaction drives the fault into criticality. The criterion for fault slip in the geomechanical model is simplified to the Mohr-Coulomb criterion, which predicts slippage when the ratio of shear stress to effective normal stress exceeds the friction coefficient:

$$\frac{\tau}{\sigma_n - p} > \mu \tag{4}$$

The driving force in induced seismicity is reservoir pore pressure, since that causes changes in total stress and shear stress by reservoir volume change. However, the local pore pressure in the fault zone is also crucial since it may destabilize faults.

Previous studies [7, 8] (showed that slip on the faults has a significant effect on the final stress state. Assuming the stress effect from the earthquakes is frozen over a long period, a large area on the fault will remain close to the critical state.

In order to relate the micro-seismic activity to the average stress computed by the model, we define a critical stress ratio over a large area (corresponding to the critical area after depletion). This normalized critical stress ratio, $R_{c,N}$, is a measure of the distance below the MC envelope over a representative area that might become critically stressed:

$$R = \frac{\tau}{\sigma_n - p} \Rightarrow \Delta R = R - \mu, \quad R_{c,N} = \frac{\int_A \Delta R dS}{A \Delta \mu} \tag{5}$$

Where μ is the calibrated friction coefficient, A is the area over which ΔR is integrated and $\Delta\mu$ is a characteristic range in friction coefficient that is used for scaling the normalized critical stress ratio. During refill, the normalized critical stress ratio becomes negative, while for small areas, slippage is still possible. Given the history of micro-seismicity, we can then relate the observed level of micro-seismicity to the forecast of the stress during future cycles. If the critical stress area over the area of interest remains below the level during the past storage cycles, it can be concluded that also the micro-seismicity will not exceed observed micro-seismic rate and magnitude.

From a general expression for the total number of earthquakes over time [9, 10], the seismicity rate can be derived for a sub-critical fault based on the Mohr-Coulomb failure function:

$$F_{MC} = \tau - \mu(\sigma_n - p) \Rightarrow$$
$$\Delta F_{MC} = \Delta\tau - \mu(\Delta\sigma_n - \Delta p) \quad (6)$$

For large slip areas this function determines failure ($F_{MC} \geq 0$), but when the average stress on the fault is sub-critical micro-seismicity is still observed and we propose that the failure of small fault patches or fault branches is related to shear strain of the fault zone.

The micro-seismic rate is then related to changes in shear stress:

$$N = k\iint_{A_c} F_{MC} H(F_{MC})\, dSdt \Rightarrow$$
$$N_{MS} = k\iint_{A_c} \Delta\tau P(R_{c,N})\, dSdt \quad (7)$$
$$\frac{dN_{MS}}{dt} \propto \int_{A_c} \frac{d\Delta\tau}{dt} P(R_{c,N})\, dS$$

Where N is the total number of earthquakes induced on a fault that reaches the MC condition, given by the Heaviside step function, H, of the MC failure condition and N_{MS} is the total number of micro-seismic events, P is the probability of occurrence as function of average critical stress ratio and k is a matching parameter. The micro-seismic rate is determined over the largest contiguous critical area A_c. The usual condition for slippage given by the Heaviside step function of the failure function is replaced with a probability of the average critical stress ratio, in which the possibility for occurrence of micro-seismicity is extended to faults that are on average sub-critical.

For a Gaussian distribution of strength of the fault, the probability would fall off rapidly with average stress:

$$P = 0.5(1 - P_{res})\left(1 + erf\left(aR_{c,N}\right)\right) + P_{res} \quad (8)$$

Where a is a match parameter and P_{res} is the residual probability at low stress. The probability approaches 1 for critical stress ratio equal to the friction coefficient, but falls off rapidly for sub-critical stress.

This analysis is linked to the estimate of maximum magnitude in two ways: a large earthquake requires a large critically stressed area and the usual Gutenberg-Richter (GR) correlation that relates the rate of seismic activity with magnitude. It is doubtful that the standard GR relation applies to induced seismicity, since during depletion 4 large earthquakes were observed while there was a lack of smaller earthquakes which should have been observed according to the GR relation. On the other hand, the GR relation can be used to determine the probability of strong events from the micro-seismic activity. At least in some gas fields this provides a conservative estimate of the chance of large earthquakes. An increase in micro-seismic activity can then be interpreted as a warning signal for larger earthquakes.

4. Calibration and Stress Simulations

The match of the subsidence during depletion and refill/storage is first used to determine reservoir stiffness.

Table 2 lists the resulting calibration coefficients. For calibration of the depletion phase, the difference in stress state between virgin and depleted state in 2007 results in a poroelastic coefficient of 0.79. The observed surface subsidence during depletion determined the compaction coefficient (5 x 10^{-11}[1/Pa]). Poisson's ratio was set as the remaining degree of freedom. Because of the high value of the poroelastic coefficient the range for Poisson's ratio was a priori limited to [0, 0.175].

Table 2. *Calibrated coefficients. the grain compaction modulus c_g, the Poisson ratio v, the Young's modulus E, the biot coefficient, the Poroelastic coefficient A_p and the compaction modulus c_m, τ is the relaxation of the Kelvin-Voigt viscoelasticity.*

Phase	A_p	c_m	v	c_g	E	α_B	τ
	(-)	(1/Pa)	(-)	(1/Pa)	(GPa)	(-)	(days)
Depletion 1971-2007	0.79	5 x 10^{-11}	0.175	10^{-13}	18	1	N/A
Refill and storage 2007ff	0.92	2 x 10^{-11}	0.07	10^{-13}	48	0.998	69

For the refill and storage period, the compaction modulus follows from the Geodetic and GPS measurements (2 x 10^{-11}[1/Pa]). This is a reduction in the compaction coefficient by a factor 2.5 compared to the depletion. The grain compaction coefficient is considered to be constant over the lifetime of the reservoir and hence determined by the depletion phase.

The absence of large magnitude seismicity during refill and storage required that the stress path in the middle of the reservoir during refill and storage does not show hysteresis compared with the depletion phase; only the stiffness shows hysteresis. The usage of an alternative stress path would result in seismicity of considerable magnitude during refill/storage

which contradicts observation.

The refill stress path resulted in a poroelastic coefficient of 0.92, which limits the choice for the Poisson ratio during depletion to [0.15, 0.175]. This is because a high poroelastic coefficient in combination with compaction coefficient of 2 x 10^{-11} is only possible for grain compaction coefficients of 5.2 x 10^{-13} or smaller. For higher values the Poisson ratio would become negative. Within this narrow range, the Poisson ratio for the depletion coefficient was set to 0.175. The latter gives a depletion Young's modulus of 18 GPa which corresponds to the value used in earlier studies.

Finally the relaxation time in the Kelvin-Voigt model was set to 69 days, obtained from a weighted average of the relaxation times observed in 4 GPS stations.

Figure 6 compares the resulting stress path in the middle of block 1 M to the original elastic stress path. The fully elastic stress path is free of hysteresis which indicates limited pressure diffusion effects. For the inelastic simulation, during refill, the horizontal stress recovery is equal to the stress during depletion. For seismic risk, this is the best case since in some reservoirs stress has not recovered during pressure increase, which would give higher shear stress. However, if other effects, such as fault slip can explain observed micro-seismicity it is better to assume full stress recovery to keep the model as simple as possible.

Table 3 lists the average formation stresses. The virgin vertical stress distribution is close to a uniform increase with depth away from the faults. Non-uniformity in rock properties and stress initialization introduce stress rotations and stress discontinuity close to faults and domain transitions. Gradients are about 22-23 kPa/m in the center of the blocks, while they vary in between 20-25 kPa/m close to the faults.

Table 3. *Geomechanical Properties for populating the model at virgin conditions.*

Formation		**ρ_B**	**E**	**ν**	**α_B**	**G_p**	**$G_{\sigma min}$**	**$G_{\sigma max}$**	**$G_{\sigma V}$**
		kg/m^3	**GPa**	**(-)**	**(-)**	**kPa/m**	**kPa/m**	**kPa/m**	**kPa/m**
North Sea	NS	2200	0.5	0.25	0.7	10	14.9	19.5	22
Vlieland Claystone	KN	2300	10	0.25	0.7	10	15	19.7	22
Upper Germanic Trias	UGT	2300	10	0.25	0.7	10	15.2	19.9	22
Lower Germanic Trias	LGT	2400	20	0.25	0.7	10	15.3	20.1	22
Zechstein Salt	ZET	2160	35	0.3	0.7	10	22.3	22.3	22.3
Zechstein Platten Dolomite and Anhydrite	ZEB	2600	43	0.25	0.7	10.5	20	20	22
Rotliegend	RO	2500	18	0.12	1	10.4	15.5	20	23
Carboniferous	BU	2600	30	0.2	0.7	10.5	16	21	23
Underburden	UB	2600	30	0.2	0.7	10.5	16	21	24

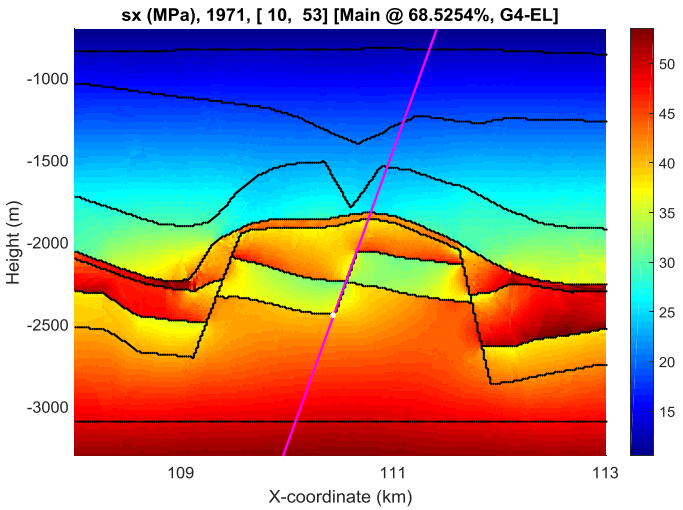

Figure 7. *Initial minimum horizontal stress and (right) initial minimum horizontal stress gradient. Pink line is line parallel to the midfield fault.*

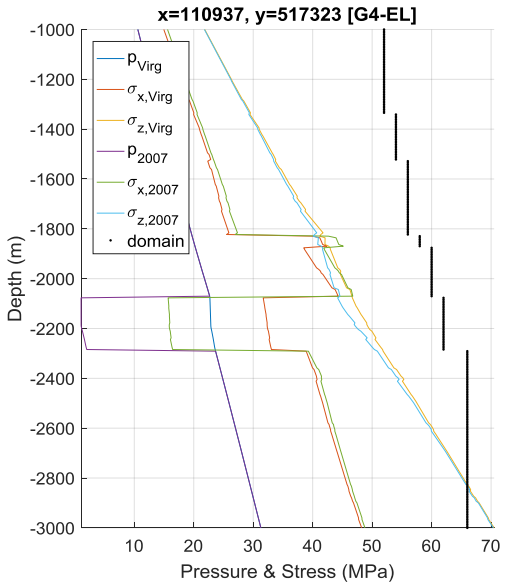

Figure 8. *Pressure and stress vs depth in the centre of the reservoir.*

The minimum horizontal stress gradient is about 15-16 kPa/m except in the Anhydrite/Carbonate formation (20 kPa/m) where it is at 90% of the vertical stress gradient and in the Salt layer (Figure 7) where it is close to the vertical stress gradient (23 kPa/m). This gives minimum horizontal over vertical stress ratio's in between 0.65-0.7 in the model, except for the salt layers that are calibrated to unity and in the Anhydrite/Carbonate that is calibrated at a ratio of 0.9, see Figure 8.

4.1. Depletion Phase Simulation

The pressure history is plotted in Figure 9 with discrete points at which the Eclipse simulation output was sampled. For an elastic model (and without salt creep) there is no time dependence, so the stress simulation consists of a succession of stationary steps with the pressure applied as external stress.

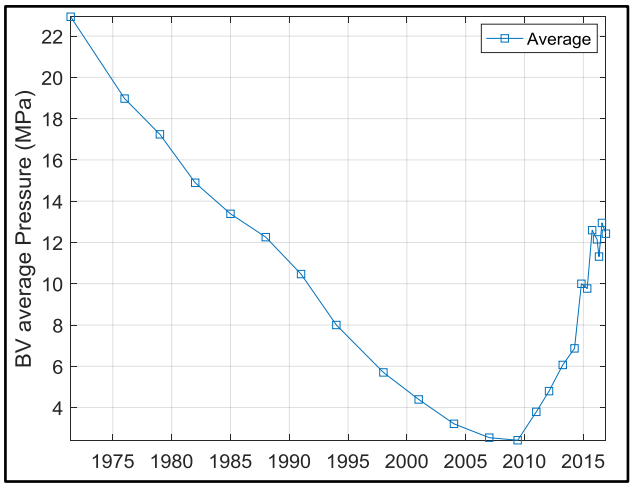

Figure 9. *Average gas pressure evolution used for the elastic simulation.*

The elastic stress forms the basis of all further work and can tell whether some unexpected observations of micro-seismicity can just be explained with an elastic model. For instance, the refill seismicity occurred while the pressure difference on the Midfield fault was running quite high which might cause criticality of the fault.

Figure 10 shows the critical stress ratio (shear stress/effective normal stress) along the Midfield fault, on both sides of the fault plane. At the fault plane, there is a discontinuity in stress since the pore pressure is discontinuous as are the rock properties. Although the FEM ensures equilibrium, there will be stress discontinuities due to material property contrast as well as numerical errors. So, the stress was computed on both sides of the fault plane at a small distance from the plane.

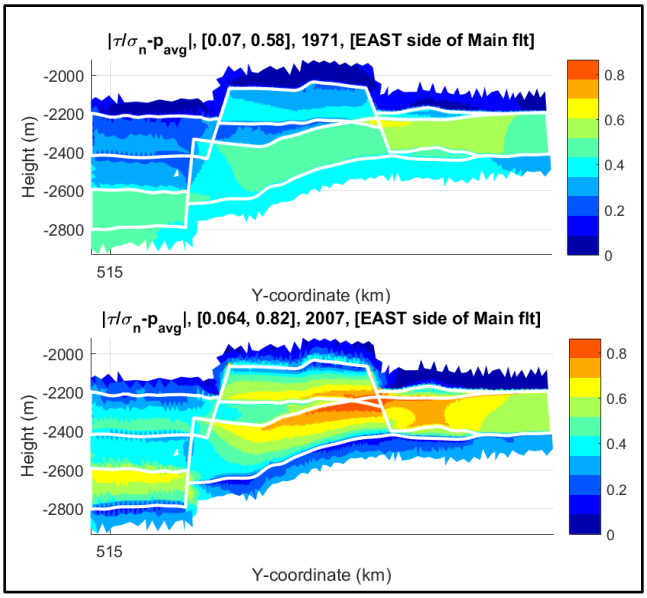

Figure 10. *Critical stress ratio on East side of the Midfield fault at different times, using averaged pore pressure in the fault. In the header of each plot, critical stress ratio, minimum and maximum value, the year, and the side of the fault.*

The pore pressure in the fault zone is unknown, so it is justified to treat this as a matching parameter. For the Midfield fault, it is natural to use average pressure where reservoir sands connect. However, at the East fault, the reservoir is bounded by non-reservoir layers. It is known from seismological research that damage zones at fault zones are about 1% of fault length, so the thickness should be about 10 m, and a core sliding zone of 10-20 cm. Even with permeability as low as 1 microD such a fault zone should be quickly depleted. That implies that taking average pressure is an upper limit of the actual pressure. It turned out that using minimum pressure for the East fault made only a minor difference since the critical area is partially below the reservoir so that pore pressure is determined by non-reservoir

rock layers that do not deplete with the reservoir.

On the Midfield fault, the critical stress ratio depends strongly on the choice for the fault pressure. Taking average pressure will yield a lower estimate of critical stress ratio.

In Figure 10, we see a stress concentration near the scissor point where the sands get separated by the fault throw. This is due to superposition of the differential compaction effect from both reservoir blocks. However, the stress concentration only becomes visible when using the averaged fault zone pressure. The full picture of the stress concentration in a cross-section through the fault at the scissor point is shown in Figure 11. The largest change in critical stress is seen at the non-reservoir side of the fault, because of the high pore pressure that gets close to the stress, so that effective stress becomes very small. Using average pressure on the fault plane yielded the best match with observations, so in the remainder of the simulations, the average pressure will be used.

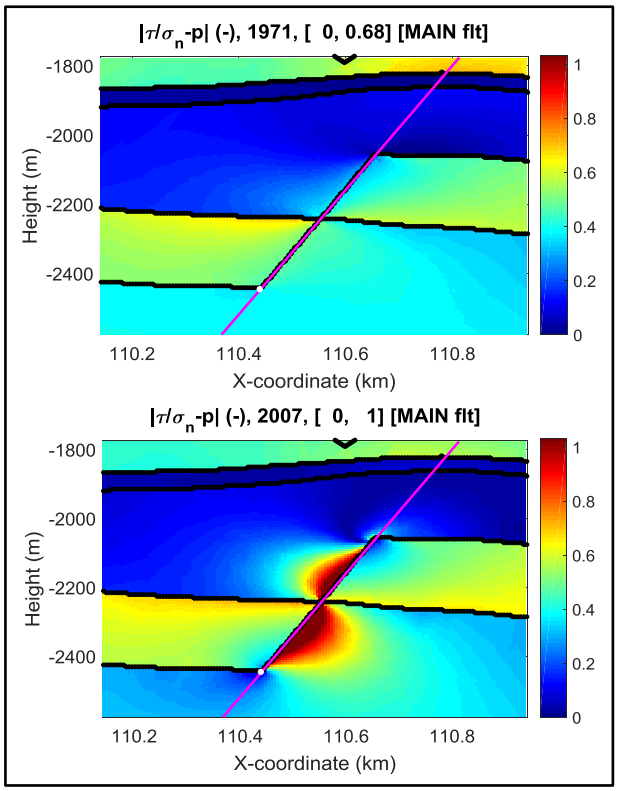

Figure 11. *Critical stress ratio in a cross-section through the Midfield fault at different times, using local pressure. In the header of each plot, critical stress ratio, the year, minimum and maximum value and the fault name. At the time of the first earthquake in 1994, the critical stress ratio had already reached 0.83.*

The next step is to determine the area of the fault above a certain threshold friction coefficient. Faults are very heterogeneous, but it is known from seismology that large earthquakes can only occur if a contiguous area of the fault zone becomes critically stressed. Moreover, detailed studies have shown that slip is confined to such a high stress area [11, 12, 13]. So, one of the objectives of stress analysis is to determine the maximum size of such stressed regions.

Since the total seismic moment associated with the depletion earthquakes will significantly affect the state of the shear stress at the start of the refill, the next section will correct the stress during depletion for the seismic slip of all the depletion earthquakes. The friction coefficient will be calibrated on the cumulative seismic moment.

4.2. Stress Simulations Including Slip Correction

During depletion four earthquakes exceeding magnitude 3 occurred at the midfield fault (see Table 4). A magnitude 3 event involves a slip area of order 10^5 m^2, which is a significant fraction of the total fault area that is in contact with the reservoir. The (seismic) slip associated to these four events should be explicitly accounted for, since it will significantly affect the state of the shear stress at the end of depletion and during refill.

Table 4. *Seismic event during depletion, their magnitude (M_w), seismic moment (M_0) and the cumulative seismic moment (ΣM_0).*

Date	M_w	M_0 (Nm)	ΣM_0 (Nm)
1994-08-06	3	4.00E+13	4.00E+13
1994-09-21	3.2	7.00E+13	1.10E+14
2001-09-09	3.5	1.90E+14	3.00E+14
2001-09-10	3.1	6.30E+13	3.63E+14

4.3. 2D Slip Modelling Results

A 2D steady state slip model was constructed at the most critical point at the midfield fault in the 3D model, (see Figure 12). Mohr-Coulomb friction was applied on the fault with the friction coefficient obtained from the dynamic friction coefficient. The model was calibrated in the same way as the 3D model such that the critical stress ratio of the 2D model is representative for the 3D case. In the 2D model, slip is modelled as a continuous process, but such that the cumulative shear moment in 2001 equals the cumulative seismic moment of the depletion Earthquakes.

When slip occurs, the shear stress at the center of the slip area is reduced, such that the Critical Stress Ratio (CSR) does not exceed the MC failure envelop, while the stress at the edge of the slip area increases (Figure 13) moving it in the direction of the failure envelop. The excess shear, being the difference between the shear stress for a simulation with slip and an elastic simulation, is zero when averaged over the height. As a consequence, the area over which the fault becomes critical is larger when slip is included (Figure 13). During slippage, the normal fault stress does not change and remains the same as in the elastic simulation.

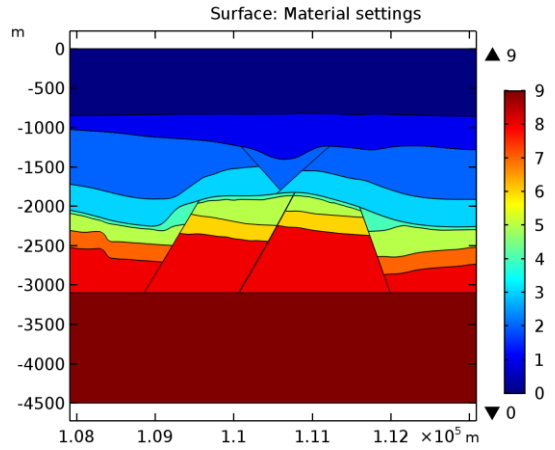

Figure 12. *Geology of the 2D model. 2D model is a cross section at the most critical point at the midfield fault of the 3D model.*

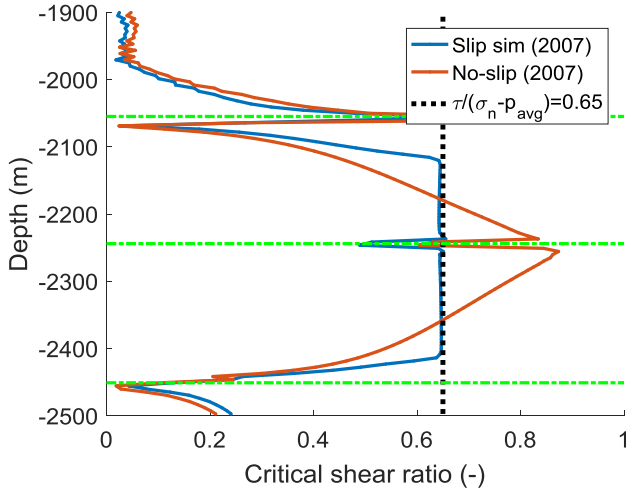

Figure 13. *Comparison of the critical stress ratio between a slip simulation with friction coefficient of 0.65 and elastic simulation without slip at the end of depletion 2007.*

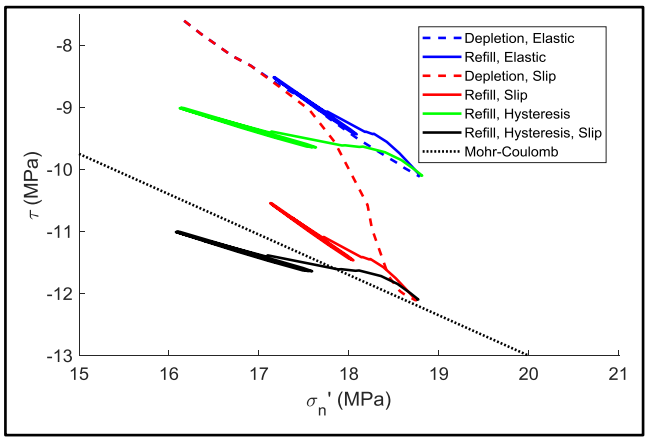

Figure 14. *Mohr-Coulomb plot of depletion and refill phases for different behavior at a point just below the critical region, at 2400 m depth. With hysteresis during refill, the stress moves towards the failure line and slip causes the point to become critical, so that during refill the area of the fault at the bottom of the slip region becomes again critical.*

The change in shear stress by slip introduces stress path hysteresis for the points affected (Figure 14), as shown for a point on the fault at 2400 m depth. While this point remains non-critical in the elastic solution, the shear stress redistribution resulting from the slip pushes this point towards the failure envelop (similar to the zones just below and above the critical stressed are in the elastic solution in Figure 13) If one also accounts for the stiffer response during refill, the MC failure gets even exceeded (Figure 14), because coefficient hysteresis results in lower normal stresses at the rim of the depletion slip area.

4.4. Slip Modelling in 3D

The effect of a shear fracture is added to the stress computed with the three-dimensional model, as based on the 2D simulations and theoretical solutions for shear fractures [14]. The theoretical solutions for shear fractures [15] give a stress change at a distance r from the fracture that is proportional to the well-known $1/\sqrt{r}$ dependence. For constant slip, the stress would be singular, but with slip falling to zero at the edges of the fracture, the singularity is relieved. So, a small amount is added to the distance from the fracture in order to avoid the singular behavior. Using these solutions, we can develop an estimate of the shear stress change in the 3D model due to slippage derived from the elastic simulation, see Figure 15.

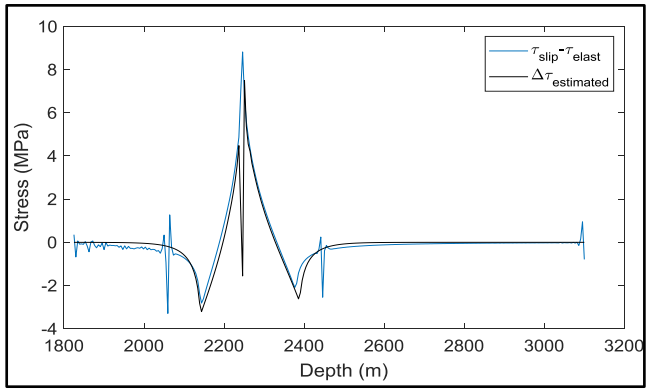

Figure 15. *Slip stress computed in 2D simulation showing the additional shear stress due to slip from the simulation (τ_{slip}-τ_{elast}) as well as the estimated excess shear stress due to slip ($\Delta\tau_{estimated}$), derived from the elastic stress. The discontinuities occur at domain boundaries and are numerical artefacts.*

Based on the shear stress correction we also estimate the slip, using the theoretical relations and the 2D simulations. The average slip is then correlated to the maximum shear stress correction.

In the 3D simulations there is both a dip-slip and strike-slip component and the correction is done separately for both components. It turned out that most of the slip was in the dip-slip direction, with only a small strike-slip component.

Performing the procedure for the 3D simulations, the slip

area is indeed enlarged, especially above and below the most critical point; i.e. where the opposite blocks are just separated.

4.5. Slip and Maximum Magnitude During Depletion

The stress due to the shear dislocation can be correlated to the slip, so that an estimate is obtained of the maximum seismic moment and magnitude. Seismic moment in this section and the remainder of the document is computed via $GA_{slip}\bar{u}_{slip}$, with $\bar{u}_{slip}$ the average slip obtained from the excess shear stress, A_{slip} the slip area and G the shear modulus.

This can be used to calibrate the model during depletion on the cumulative seismic moment that was observed in the four earthquakes. Using the computed slip yields a low estimate of the seismic moment, since the stress drop is small. However, it is consistent to calibrate the model on the computed slip and then use any slip that may occur in the refill phase to predict the seismic magnitude.

In previous work on Bergermeer fault slip [16, 8], the computed maximum slip varied strongly between 120 and 20 mm, in a 2D and 3D model, respectively. The current slip estimate falls in between these extremes, as listed in Table 5. For consistency, it is necessary to use the computed slip for magnitude estimates, because incorporating slip results in a large section of the fault that may be critically stressed but that doesn't necessarily result in large earthquakes. A large earthquake can only be induced if there is sufficient excess shear stress resulting in potential slip. It will be shown that during refill a large patch becomes critical, but with small excess stress so that the maximum seismic moment is still small.

Table 5. *Size of slip area, average slip and moment magnitude in depletion and refill simulations.*

Case	Slip Area (km^2)	Average slip (mm)	Moment Magnitude
Depletion	0.6	20	3.5
Refill without slip correction	0.05	3	2.2
Refill with slip correction	0.05	0.2	1.5

The calibrated friction coefficient was determined as 0.65. It is possible that part of the slip was non-seismic or below the detection limit, so the critical area was also computed for a lower friction coefficient of 0.6. In that case, the seismic moment would be a bit larger for the lower friction coefficient.

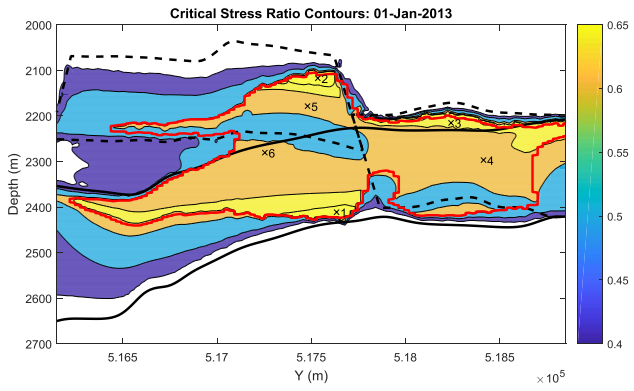

Figure 16. *Contours of critical stress ratio on the Midfield fault, just before the time of the largest micro-seismic event. The only critically stressed patches occur at the boundaries of the maximum slippage area.*

At the start of refill a large area is still critical and Figure 16 shows that even at higher pressure in 2013 some areas remained critically stressed. In this simulation, the slip was applied continuously, so that the stress state remains at or below the MC-envelop. Of course, this would not cause large earthquakes since that would require excess shear stress above the MC envelope. However, it can explain small micro-seismic events which represent only small slippages and energy release. The critically stressed regions are caused by the additional shear stress around the area that slipped in the depletion earthquakes.

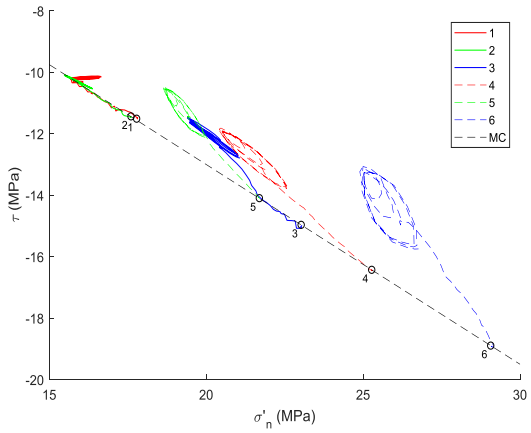

Figure 17. *MC plot of selected points on the fault, shown in Figure 16.*

Figure 17 show the stress evolution of 6 selected points on the fault (indicated in Figure 16). Points 1-3 are on the critically stressed regions caused by the additional shear stress, while points 4-6 are near the middle of the fault. Point 5 is near the juxtaposition point, where both fault blocks separate.

There is a distinct behavior for points 1-3 compared with points 4-6. The latter points show immediate stabilization because the stress moves away from the failure envelope. The points near the regions that were critically stressed by additional shear stress remain for a while on the envelope. Points 1-2 even remain close to the envelope during the cycles. Finally, cumulative slip during storage cycling stabilizes these regions.

We will now consider the predicted maximum magnitude from critically stressed fault area and the predicted seismic rate. This is done both for the low-storage case with maximum pressure of 133 bar and for the high-storage case with 150 bar maximum pressure.

Figure 18 shows both the maximum magnitude (upper graph) based on the peak in critical stress ratio as well as the averaged critical stress ratio (lower graph). The maximum magnitude during refill and storage cycles remains below magnitude 1.5, which corresponds to a small excess shear stress on the critically stressed area.

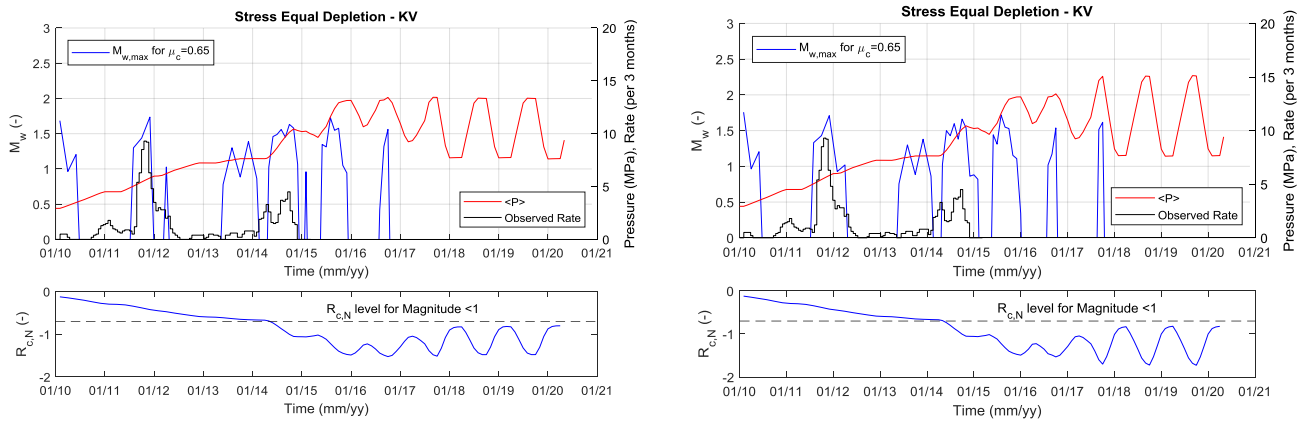

Figure 18. *Magnitude from slip for the Midfield fault with average gas pressure and observed micro-seismic rate (upper graphs) for (left) the 133 bar case (right) the 150 bar case. Rate is defined as events per 3 months times 0.1. The lower graphs show the average critical stress ratio. This ratio remains below the level of the maximum recorded historical micro-seismic event of magnitude 1.*

Micro-seismic activity ceased after 2014 which agrees qualitatively with the falling trend in maximum magnitude and the drop in average critical stress level. Apart from the history, also future cycles are shown over the full pressure range between 77 and 133 bar and between 77 and 150 bar for the enhanced storage case. Moreover, these forecast cycles use the maximum available injection and production rate. The maximum magnitude occurs during injection and at high pressure, while the average critical stress ratio is highest at low pressure, as would be expected. The reason for this counter intuitive behavior of the peak stress is caused by a relatively constant shear stress. The normal stress fluctuates with the reservoir pressure, giving a fluctuation in critical stress ratio at the critical point and even an excess over the MC envelope. The excess shear stress gradually disappears by continued slip and the critical point stabilizes, so that the maximum magnitude drops with subsequent cycles.

Using the expression for the seismic rate in terms of the rate of change of shear stress and the probability function of critical patches (eq. 7), the observed rate can be matched as shown in Figure 19 The change in seismic rate is caused by a fault that stabilizes on average (reduction of $R_{c,N}$ giving a lower probability of seismicity) a shear rate that scales proportionally to the pressure rate. The match is only qualitative, but the response of seismicity rate to changes in shear stress is reflected in the predicted rate and the disappearance of seismicity can be matched with the assumption that the probability of critically stressed areas falls with the gradual stabilization of the fault. The model predicts that the seismicity would again increase during the cycles at full capacity. In these cycles, the shear rate will be much higher and also the critical stress ratio would be less negative since the pressure is lower than attained during the historical cycles. Still, the micro-seismic rate is predicted to remain low compared with previous activity. Moreover, the peak in the critical stress remains below the critical level for felt earthquakes. So, the model only predicts some weak micro-seismic events that pose negligible risk.

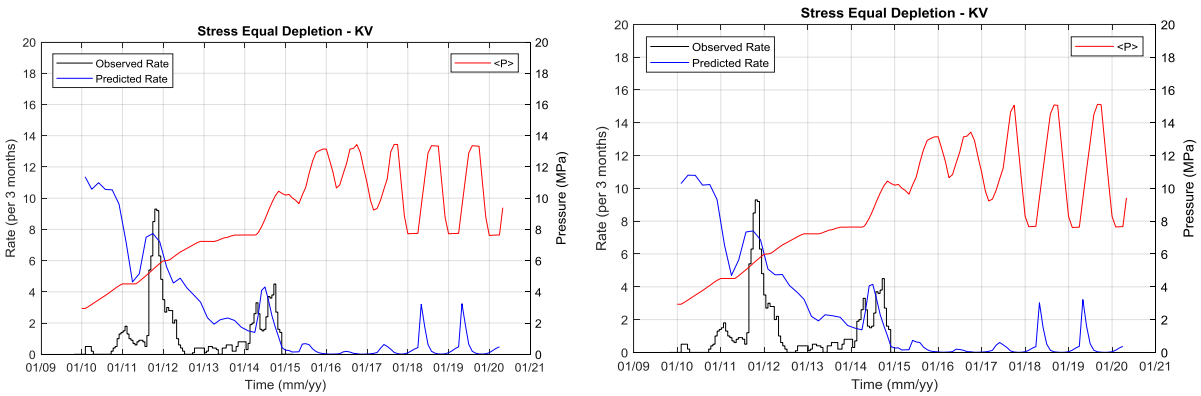

Figure 19. *Micro-seismic rate and predicted rate that is derived from the shear stress rate and the stress level on the fault. Rate is defined as event per 3 months times 0.1. The predicted rate was calibrated on the absence of micro-seismicity after 2014. Refill, storage and (left) 77-133 bar forecast cycles and (right) 77-150 bar forecast cycles.*

5. Discussion and Conclusions

For Bergermeer gas storage, a new geomechanical model has been calibrated to all available measurements. This yielded a model that matches the observed seismicity. By proper calibration, the model establishes the link between observed and predicted seismicity. That is relevant for assessing the risk of future storage cycles.

In principle, faults that reach criticality can fail either in a creeping fashion or by releasing elastic energy generating seismic waves. Considering that most gas fields do not induce felt earthquakes, while the differential compaction effect should be strong enough to cause slippage on any faults, it is possible that on many faults the slip occurs non-seismically. For safety analysis, this means that slippage may go unnoticed, which is not much of a concern, except that under some conditions the fault might become seismic and still induce an earthquake. In the Bergermeer reservoir there are three main faults that were all critically stressed during initial depletion. However, only the Midfield fault induced felt earthquakes. It is commonly observed in gas storage reservoirs that faults which have induced earthquakes during depletion are also active during storage cycles. That would imply seismic activity on the East fault during depletion, but probably at such a low level that this activity was never felt or detected, implying a magnitude below 1.5. The West fault was critically stressed but showed no activity at all, indicating that it is non-seismogenic. It may have slipped in a creeping fashion, but could also have remained inactive because of high strength of the fault.

An important observation is the large gap between depletion seismic intensity and the much weaker micro-seismicity observed in the refill and storage phases. Weak micro-seismic events are commonly observed in underground formations when strain is applied, because rock formations deform with micro-fracturing. Moreover, rock formations are heterogeneous and small critically stressed faults are ubiquitous. Slippage areas of less than a few square meters generated these small micro-seismic events which are of no concern to seismic risk. Looking at the micro-seismic character it is possible to dismiss the micro-seismicity as just a secondary effect of the critical stress acquired during the original depletion. The micro-seismic analysis showed that no contiguous areas of the fault became critical, but just some scattered patches. On the other hand, the larger micro-seismic events correspond to slippage areas at reservoir scale, so that it appears justified to interpret them as a potential warning signal of fault instability.

Seismic risk during refill, storage and forecast

Assuming that during depletion the Midfield fault has slipped to a stable configuration, given by a single friction coefficient, it is possible to compute the stress distribution. A crucial feature of slippage is that not only the peak in shear stress is reduced, but the shear stress is increased at the edges of the slip area. If the stress due to depletion slippage is frozen in, the additional shear stress causes criticality of the fault during refill of the reservoir. Since the critical area during refill is about 10% of the total slippage area during depletion, the surface area alone suggests potential for quite strong earthquakes. However, during storage, the excess shear stress above the failure condition in this area is rather small, so the magnitude of the potential earthquakes is also small. The best match with the observations is obtained when the fault is assumed to slip when it becomes critical. That can explain the disappearance of seismicity over time during successive storage cycles.

The model was calibrated to observed seismicity to forecast the expected fault behavior during future storage cycles. For the Midfield fault, it is expected that little seismicity will be induced during future cycles, since the pressure cycles will cause some slippage of the fault that renders it more stable. The East fault is predicted to remain stable during the storage cycles, although micro-seismicity is still possible. Heterogeneities may slip and at higher injection rate the seismic rate may also increase, but the micro-seismicity will have a small magnitude.

Seismic risk based on Seismic Observations

For assessing risk, it remains most relevant to directly consider the information from the micro-seismic observations. That yields a reassuring conclusion in view of the quantity as well as quality of micro-seismicity. Of most concern at the start of the project was seismic activity on the Midfield fault and this indicated only scattered patches where the fault slipped during refill. Since there is no indication of a large contiguous critical area, it is unlikely that large seismic events could be induced. Moreover, the activity on the Midfield fault has completely ceased after reaching 100 bar reservoir pressure.

The Bergermeer case presents a full data set on gas storage behaviour, which is also relevant for upcoming CCS projects. Storage in depleted gas fields resembles cushion gas injection in a gas storage. For design of CCS projects, it is particularly relevant that stress recovery appears to be complete. For potential thermal fracturing it is relevant that reservoir stiffness is enhanced which enhances the potential for fracturing.

The following is concluded from this study:

1. The geomechanical response of the reservoir has been analyzed based on the relation between stress, surface displacement and seismicity:

(1) Calibration of the friction coefficient yields a value of 0.65 for the midfield fault. The model then gives a cumulative seismic moment equivalent to the observed seismic moment. A smaller friction coefficient is also possible, but in that case the match with refill seismicity becomes poorer.

(2) Most seismic activity since 2007 occurred during cushion gas injection. The activity was much weaker during the fast pressure increases during storage cycles and the activity on the Midfield fault has ceased. Therefore, the fault systems are stabilizing, which is explained by average stress recovery on the fault and continuous slippage.

(3) Refill seismicity on the Midfield fault can be explained with the additional shear stress induced by slip from the depletion earthquakes.

a) Disappearance of seismicity on the Midfield fault can be matched by assuming continuous slip on the fault when it becomes critical. Much of this slip should be non-seismic since the micro-seismicity accounts only for a few percent of the potential slip.

b) The pressure differential between the two compartments had a minor effect on seismicity.

c) For the best match no seismicity is expected for the Midfield fault during future storage cycles.

2. Seismic risk is deemed small for future gas storage cycles. This conclusion is supported both by observation and the calibrated model.

Assuming a worst case that no slip has occurred on the Midfield fault during refill and storage cycles, the maximum possible magnitude for an earthquake during future storage cycles is 2.2.

Abbreviations

BU	Carboniferous
FEM	Finite Element Method
KN	Vlieland Claystone
KV	Kelvin-Voigt
LGT	Lower Germanic Trias
LOT	Leak-off Test
NS	North Sea
RO	Rotliegend
UB	Underburden
UGT	Upper Germanic Trias
ZEB	Zechstein Platten Dolomite and Anhydrite
ZET	Zechstein Salt

Author Contributions

Cas Berentsen: Conceptualization, Formal Analysis, Software, Writing – original draft

Hans De Pater: Conceptualization, Formal Analysis, Software, Writing – original draft

Conflicts of Interest

The authors declare no conflicts of interest.

Appendix

Table 6. *Nomenclature.*

Variable	Description	Units	Dimensions
A_p	Poroelastic coefficient	[-]	(-)
A	Area	[m^2]	(L^2)
c	cohesion	[MPa]	(m/Lt^2)

Variable	Description	Units	Dimensions
c_g	grain compressibility	[1/MPa]	(Lt^2/m)
c_r	rock compressibility	[1/MPa]	(Lt^2/m)
c_m	compaction coefficient	[1/MPa]	(Lt^2/m)
E	Young's modulus	[GPa]	(m/Lt^2)
E_{eff}	Effective Young's modulus	[GPa]	(m/Lt^2)
G, G_{EL}	Shear modulus	[GPa]	(m/Lt^2)
g	Stress gradient	[kPa/m]	(m/L^2t^2)
H	Height	[m]	(L)
L_z	Characteristic height	[m]	(L)
K_h	horizontal stress ratio	[-]	(-)
M_0	seismic moment	[N m]	(mL^2/t^2)
M_w	moment magnitude	[-]	(-)
p	pressure	[MPa]	(m/Lt^2)
$R_{c,N}$	average critical stress ratio	[-]	(-)
t	time	[s]	(t)
u	displacement vector	[m]	(L)
u_{slip}	displacement in dip direction	[m]	(L)
u_{strike}	displacement in strike direction	[m]	(L)
V_{res}	reservoir volume	[m^3]	(L^3)
α_B	Biot coefficient	[-]	(-)
ν	Poisson's ratio	[-]	(-)
μ	friction coefficient	[-]	(-)
σ_d	Deviatoric stress	[MPa]	(m/Lt^2)
$\sigma_{H,max}$	maximum horizontal stress	[MPa]	(m/Lt^2)
$\sigma_{H,min}$	minimum horizontal stress	[MPa]	(m/Lt^2)
σ_{vert}	Vertical stress	[MPa]	(m/Lt^2)
σ_n	Normal stress on fault plane	[MPa]	(m/Lt^2)
τ	Shear stress	[MPa]	(m/Lt^2)

Units: SI (m= metre, s= second, kPa =10^3Pa, MPa =10^6Pa, GPa =10^9Pa)
Dimensions: m= mass, L= length, t= time

References

[1] Haak, H. W., B. Dost, F. H. Goutbeek (2001), "Seismische analyse van de aardbevingen bij Alkmaar op 9 en 10 september en Bergen aan Zee op 10 oktober 2001", KNMI Technical report; TR-239.

[2] Q-con (2019), https://www.taqainnederland.nl/wp-content/uploads/2019/07/Induced-Seismicity-in-the-Bergermeer-field-Hypocenter-Relocation-and-Interpretation.pdf

[3] Wassing, B. B. T., Orlic, B., Leeuwenburgh, O., Geel, C. R., (2011), "3D Geomechanical Modelling of Fault Stability in the Bergermeer Field During Underground Gas Storage Operations", TNO-060-UT-2011-01388/C, 31 August 2011.

[4] Baker RDS, (2011), "Dynamic Geomechanical Modelling of the Bergermeer Underground Gas Storage, Netherlands", Part 1 – Base Case Modelling, Part 2 – Scenario Modelling, version 2011 09 22.

[5] Fenix, (2018), '3D Geomechanical Model for Gas Storage Bergermeer'. TAQA Energy BV, https://www.taqainnederland.nl/wp-content/uploads/2018/03/TEN_DM-191618-v1-3D_Geomechanical_Model_Gas_Storage_Bergermeer_77_-_133....pdf

[6] Roest, J. P. A., Kuilman, W. (1994). Geomechanical analysis of small earthquakes at the Eleveld gas reservoir. In: 'Eurock '94; SPE/ISRM international conference, Delft, Netherlands', pp. 573–580.

[7] Muntendam-Bos, A. C.,, B. B. T. Wassing, K. van Thienen-Visser, (2009), Effects of differential pressures across the central Bergermeer fault", TNO-034-UT-2009-00171/B 16 January 2009.

[8] Orlic, B., Wassing, B. B. T. and Geel, C. R., (2013), "Field scale geomechanical modeling for prediction of fault stability during underground gas storage operations in a depleted gas field in the Netherlands", Proc. 47th US Rock Mechanics / Geomechanics Symposium held in San Francisco, CA, USA, 23-26, June 2013.

[9] Harris, R. A., (1998), "Introduction to special section: Stress triggers, stress shadows, and implications for seismic hazard", Journal of Geophys Research, V 103, B10, P24, 347-24, 358.

[10] Dempsey, David, Jenny Suckale, (2017), "Physics-based forecasting of induced seismicity at Groningen gas field, the Netherlands", Geophys. Res. Lett., 44, https://doi.org/10.1002/2017GL073878.

[11] Baisch, S., and H.-P. Harjes, 2003. A model for fluid injection induced seismicity at the KTB. Geophys. Jour. Int., 152, 160-170.

[12] Baisch, S., Carbon, D., Dannwolf, U., Delacou, B., Devaux, M., Dunand, F., Jung, R., Koller, M., Martin, C., Sartori, M., Secanell, R., and R. Vörös, 2009. Deep Heat Mining Basel - Seismic Risk Analysis. SERIANEX study prepared for the Departement für Wirtschaft, Soziales und Umwelt des Kantons Basel-Stadt, Amt für Umwelt und Energie, 553 pages.

[13] Baisch, S., Vörös, R., Rothert, E., Stang, H., Jung, R., and R. Schellschmidt, (2010), "A numerical model for fluid injection induced seismicity at Soultz-sous-Forêts.", International Journal of Rock Mechanics and Mining Sciences 47, 405-413 https://doi.org/10.1016/j.ijrmms.2009.10.001.

[14] Westmann, R. A., (1965), "Asymmetric Mixed Boundary-Value Problems of the elastic half-space", Journal of Appl Mech, June 1965.

[15] Kassir, M. K., G. C. Sih, (1966), Three dimensional stress distribution around an elliptical crack under arbitrary loadings, Journal of Appl Mech, September 1966.

[16] Muntendam-Bos, A. C., W. B. T. Wassink, C. K. Geel, M. Louh, K. van Thienen-Visser, (2008), "Bergermeer Seismicity Study, TNO report, 2008-UR-1071/B.